

In-plane Hall effect in rutile oxide films induced by the Lorentz force

Yongwei Cui^{1†}, Zhaoqing Li^{2,3†}, Haoran Chen¹, Yue Chen^{2,3}, Yunzhuo Wu¹, Ke Pei⁴, Tong Wu¹, Nian Xie⁵, Renchao Che^{4,6}, Xuepeng Qiu⁵, Yi Liu², Zhe Yuan^{3*}, and Yizheng Wu^{1,7*}

¹Department of Physics and State Key Laboratory of Surface Physics, Fudan University, Shanghai 200433, China

²Center for Advanced Quantum Studies and Department of Physics, Beijing Normal University, Beijing 100875, China

³Institute for Nanoelectronic Devices and Quantum Computing, Fudan University, Shanghai 200433, China

⁴Laboratory of Advanced Materials, Shanghai Key Lab of Molecular Catalysis and Innovative Materials, Academy for Engineering & Technology, Fudan University, Shanghai 200438, China

⁵Shanghai Key Laboratory of Special Artificial Microstructure Materials and Technology and School of Physics Science and Engineering, Tongji University, Shanghai 200092, China

⁶Zhejiang Laboratory, Hangzhou 311100, P. R. China

⁷Shanghai Research Center for Quantum Sciences, Shanghai 201315, China

†These authors contributed equally to this work.

*Zhe Yuan, yuanz@fudan.edu.cn;

*Yizheng Wu, wuyizheng@fudan.edu.cn;

Abstract

The conventional Hall effect is linearly proportional to the field component or magnetization component perpendicular to a film¹. Despite the increasing theoretical proposals on the Hall effect to the in-plane field or magnetization in various special systems induced by the Berry curvature²⁻⁸, such an unconventional Hall effect has only been experimentally reported in Weyl semimetals and in a heterodimensional superlattice⁹⁻¹². Here, we report an unambiguous experimental observation of the in-plane Hall effect (IPHE) in centrosymmetric rutile RuO₂ and IrO₂ single-crystal films under an in-plane magnetic field. The measured Hall resistivity is found to be proportional to the component of the applied in-plane magnetic field along a particular crystal axis and to be independent of the current direction or temperature. Both the experimental observations and theoretical calculations confirm that the IPHE in rutile oxide films is induced by the Lorentz force. Our findings can be generalized to ferromagnetic materials for the discovery of in-plane anomalous Hall effects and quantum anomalous Hall effects. In addition to significantly expanding knowledge of the Hall effect, this work opens the door to explore new members in the Hall effect family.

The Hall effect describes the transverse deflection of an electric current under a perpendicular magnetic field owing to the Lorentz force and results in an electrical voltage orthogonal to the current and the magnetic field¹. It has been widely applied in magnetic field sensors and provides a general method to determine the type and density of charge carriers, such as electrons or holes, in metals and semiconductors. Subsequently, the Hall family was substantially extended by the discoveries of anomalous Hall effect¹³⁻¹⁵, the spin Hall effect¹⁶⁻¹⁹ and their quantum counterparts²⁰⁻²⁴. Understanding these transport phenomena has significantly promoted the development of modern electron theory in condensed matter physics and spintronics applications.

The conventional Hall effect is an odd function of the magnetic field, which must be perpendicular to both the longitudinal current and Hall electric field. In general, the so-called in-plane Hall effect (IPHE) is allowed by symmetry requirements with the applied magnetic field, the electric current and the Hall electric field lying in the same plane. Theoretically, Berry curvature was believed to be the key ingredient for the presence of the IPHE, which is a geometric property of electronic states resulting from relativistic spin-orbit interactions²⁻⁸. Based on this, predictions have been made in Weyl semimetals^{3,6,25}, two-dimensional electron² and hole systems⁸, and noncolinear magnetic systems^{7,12}. In experiments, Hall signals odd to the in-plane magnetic field have been observed in the Weyl semimetals WTe₂⁹ and ZrTe₅^{10,11} and in the VS₂–VS heterodimensional superlattice¹², and all these observations were attributed to the Berry curvature. Thus far, it is not clear whether the Lorenz force plays a role in the IPHE, and discovering more materials with the IPHE would certainly help in understanding the underlying physical mechanisms.

RuO₂ is a fascinating material with altermagnetism^{26,27}, which contains many interesting phenomena, such as the crystal Hall effect^{28,29} and spin splitting effect³⁰⁻³⁴. Here, we report an experimental observation of the IPHE in rutile RuO₂ and IrO₂ single-crystal films. The measured Hall resistivity is odd and linear to the in-plane field. It is also independent of the current direction and is temperature invariant. These experimental features indicate that the Lorentz force experienced by the conduction electrons is the dominant mechanism for the IPHE. First-principles calculations of nonrelativistic electron dynamics at the Fermi surface confirm the Lorentz force-induced IPHE and quantitatively reproduce the experimental observations. Based upon

symmetry analysis, we provide general and rigorous criteria for the presence of the IPHE, which is helpful for searching appropriate materials with the IPHE. Our findings can be readily extended to magnetic materials for exploration of the in-plane anomalous Hall effect and its quantum counterpart as new members in the Hall effect family.

Observation of IPHE in RuO₂(101)

First, 10 nm-thick single-crystal RuO₂(101) thin films were grown on TiO₂(101) substrates by activating sputtering in O₂ pressure, and both X-ray diffraction and transmission electron microscope measurements confirmed the high-quality epitaxial growth ([Methods and Extended Data Fig. 1](#)). Then, the RuO₂(101) films were patterned into Hall-bar structures for transport measurements under an external magnetic field, as sketched in the inset of Fig. 1a. Fig. 1a shows the typical field-dependent transverse resistivity for field **B** along the three crystal axes of [10 $\bar{1}$], [010], and [101]. In addition to the ordinary Hall effect (OHE) with the field normal to the film (**B**//[101]), an unconventional Hall signal can be observed for the in-plane field along [10 $\bar{1}$], and the IPHE is comparable to the OHE in magnitude. No Hall resistivity can be observed for the in-plane magnetic field along [010]. Systematic Hall measurements were also performed for in-plane fields with different azimuthal angles φ . Fig. 1b shows that all the Hall signals linearly vary with B, and the slope K_{ip} defined as ρ_{xy}/B can be well fitted by a cosine function (Fig. 1c). The linear field dependence of the IPHE was also demonstrated under a stronger field up to 7 T ([Extended Data Fig. 2](#)). Hall measurements were performed at different temperatures, and the determined slope K_{ip} of the IPHE signal with B//[10 $\bar{1}$] is nearly independent of temperature, which is strikingly different from the temperature dependence of the coefficient $K_{op} (\equiv \rho_{xy}/B)$ of the OHE signal. The different temperature dependencies of the IPHE and the OHE indicate the distinction between these two Hall signals.

The angular dependence of the Hall resistivity was further investigated systematically. Figs. 1e-g show the measured ρ_{xy} for a 2 T field rotating in the y-z, x-y and x-z planes, respectively. For the field rotating in the y-z plane, the Hall resistivity follows a cosine function, consistent with the classic relation $\rho_{xy} \propto B_z$ of the OHE. While the field is rotating in the x-y plane, the Hall resistivity also follows a cosine function ($\rho_{xy} \propto B_x$), which is consistent with the results in Fig. 1b. While rotating the field in the x-z plane, the ρ_{xy} data exhibit a sinusoidal function with a phase shift, which is just a superposition of the IPHE in Fig. 1e and the OHE in Fig. 1f. The full three-dimensional angular dependence of the Hall resistivity can be measured in a

vector superconducting magnet system, and the reconstructed Hall resistivity in the polar diagram in Fig. 1h shows that the maximum Hall resistivity occurs with field tilting in the x-z plane.

General properties of IPHE in RuO₂(101)

The observed IPHE shown in Fig. 1 is significantly different from the so-called planar Hall effect (PHE) that is related to the anisotropic magnetoresistance^{35,36}. Usually, the PHE in a paramagnetic material results in a transverse resistivity following the angular dependence of $\sin 2\varphi$ with its amplitude quadratic to the magnetic field B . In contrast, the observed IPHE shown in Fig. 1 is linearly dependent on B . To better separate the PHE contribution from the IPHE, the angular-dependent Hall resistivity was measured for the fields rotating in the x-y plane with different field strengths. Figure 2a shows the representative angular-dependent Hall resistivity $\rho_{xy}(\varphi)$ under a large rotating field of 7 T, which can be well fitted by the function $\rho_{xy}(\varphi) = \Delta\rho_{\text{IPHE}} \cos \varphi + \Delta\rho_{\text{PHE}} \sin 2\varphi$. The fitting coefficients $\Delta\rho_{\text{IPHE}}$ and $\Delta\rho_{\text{PHE}}$ are plotted in Fig. 2b as a function of B . $\Delta\rho_{\text{IPHE}}$ is proportional to B , while $\Delta\rho_{\text{PHE}}$ follows a quadratic dependence on B . It is worth noting that the PHE contribution even at the field of 8 T is still one order of magnitude smaller than the IPHE; therefore, it can be safely neglected in measurements with smaller fields.

The thickness-dependent IPHE was systematically investigated with a RuO₂(101) film grown into a wedge shape on a TiO₂(101) substrate; thus, all RuO₂ films with different thicknesses were prepared under the same growth conditions. As shown in Fig. 2c, both Hall resistivities of the IPHE with $\mathbf{B}/[10\bar{1}]$ and OHE with $\mathbf{B}/[101]$ first increase with the film thickness and then saturate for $d_{\text{RuO}_2} > 6$ nm. Therefore, our results indicate that the measured IPHE is a bulk property of the RuO₂(101) film.

We further investigated the relation between the IPHE and the current direction. A series of Hall-bar devices were prepared on the same sample with different current directions, which is defined by the angle ψ with respect to the $[10\bar{1}]$ axis. Fig. 2d shows the typical φ -dependent Hall resistivities $\rho_{xy}(\varphi)$ with different current orientation angles ψ . All $\rho_{xy}(\varphi)$ curves show identical amplitudes with an angular offset, which is identical to the current orientation angle, indicating that the maximum ρ_{xy} always appears for the field applied along the RuO₂[101] direction. Therefore, our results demonstrate that the IPHE in the RuO₂(101) film is closely related to the crystal structure.

The current direction-independent characteristic allows us to determine the

physical origin of the IPHE. The Lorentz force results in an antisymmetric transverse resistivity with the relation $\rho_{xy} = -\rho_{yx}$ ³⁷. In contrast, the Berry curvature-induced transverse resistivity is symmetric, with $\rho_{xy} = \rho_{yx}$. Thus, comparing the data for $\psi = 0^\circ$ and 90° in Fig. 2d suggests $\rho_{xy} = -\rho_{yx}$ for all magnetic field directions and hence the dominance of the Lorentz force contribution. In the general theory of the Hall effect³⁷, the Hall conductivity σ_{xy} arising from the Lorentz force is proportional to τ^2 , where τ is the relaxation time of conduction electrons. The longitudinal conductivity σ_{xx} is proportional to τ ; thus, it is expected that the Hall resistivity $\rho_{xy} = \sigma_{xy}/\sigma_{xx}^2$ induced by the Lorentz force should be independent of τ . This agrees with the temperature-independent feature of the IPHE signal shown in Fig. 1d with τ varied by the temperature-dependent electron–phonon scattering. Based on the above two features, we conclude that the IPHE observed in the RuO₂(101) films is mainly contributed by the Lorentz force exerted on the conduction electrons. Intuitively, the Lorentz force is not supposed to induce a Hall voltage inside the plane of the magnetic field and current direction. This puzzle can be solved by studying the IPHE in other samples with different crystalline orientations, as explained below.

Crystal symmetry relation of IPHE

In addition to the RuO₂(101) film, we also prepared RuO₂(110), RuO₂(001), and RuO₂(100) films epitaxially grown on TiO₂ substrates with the same thickness of 10 nm. The crystal structures of all these films were further confirmed by X-ray diffraction ([Extended Data Fig. 3](#)). All the films were then patterned into Hall–bar devices to measure the Hall resistivity under an external magnetic field with varying strength and direction. Figs. 3a-c show the field-dependent ρ_{xy} with the field along three mutually orthogonal directions, and Figs. 3e-g present the angular-dependent ρ_{xy} with a 1.8 T field rotating in the three planes. These measurements demonstrate that only the OHE can be observed and that the IPHE is always absent in these films. Note that the OHE signal in the RuO₂(100) film is weak at room temperature, but it is significantly enhanced by lowering the temperature, and the IPHE remains negligible independent of temperature ([Extended Data Fig. 4](#)).

The presence of the IPHE in the RuO₂(101) film and its absence in the films with other orientations can be understood from its anisotropic conductivity. Applying an electric field E_j generally induces a current density following Ohm's law $j_i = \sum_j \sigma_{ij} E_j$. Under the principal axes [100], [010] and [001] of the rutile lattice, the nonzero elements in the conductivity tensor are the diagonal ones, σ_{ii} ($i = 1, 2, 3$), which have the relation of $\sigma_{11} = \sigma_{22} \neq \sigma_{33}$. The resistivity measurements on the RuO₂(100) film further determine the relation $\sigma_{22} > \sigma_{33}$. For the (001), (100) and

(110)-oriented films, an in-plane electric field \mathbf{E} only results in an in-plane current density \mathbf{j} , as sketched in Fig. 4a ([Extended Data Fig. 5](#)). Therefore, the in-plane magnetic field \mathbf{B} cannot induce any in-plane Hall voltage perpendicular to \mathbf{E} , i.e., no Hall signals can be observed in these measurements. For the (101) film shown in Fig. 4b, the principal axes of conductivity tensors tilt away from the surface, resulting in a current density \mathbf{j}_\perp perpendicular to the film. Thus, the Lorentz force due to an in-plane magnetic field \mathbf{B} converts this perpendicular current component into the transverse Hall signal inside the film plane.

The above physical picture suggests that the IPHE in the $\text{RuO}_2(101)$ film is not relevant to its magnetic order or spin canting. This expectation is borne out by studying the IPHE in nonmagnetic rutile IrO_2 ^{31,38,39}, which has the same crystal structure as RuO_2 . The $\text{IrO}_2(101)$ film can be epitaxially grown on the $\text{TiO}_2(101)$ substrate, and the measured Hall signals plotted in Figs. 3d and 3 g confirm the existence of the IPHE and its irrelevance to magnetism. Similarly, the IPHE in the $\text{IrO}_2(101)$ film on the $\text{TiO}_2(101)$ substrate also shows temperature-independent behaviour ([Extended Data Fig. 6](#)).

Microscopic mechanism of the IPHE

The intuitive picture of anisotropic conductivity merely justifies the presence of the IPHE in $\text{RuO}_2(101)$ and $\text{IrO}_2(101)$, but it is difficult to analyse the angular dependence on the directions of the magnetic field and electrical current in our experimental measurements. The microscopic mechanism of the IPHE can be comprehensively understood within the semiclassical transport formalism, where the conductivity under a magnetic field is computed by⁴⁰

$$\sigma_{ij} = e^2 \tau \int \frac{d^3 k}{8\pi^3} v_i(\mathbf{k}) \int_{-\infty}^0 \frac{dt}{\tau} e^{t/\tau} v_j[\mathbf{k}(t)] \left(-\frac{\partial f}{\partial \varepsilon} \right)_{\varepsilon_F}. \quad (1)$$

Here, the first integral is carried out over all the electronic states on the Fermi surface, and $\mathbf{v}(\mathbf{k}) = (1/\hbar)\nabla_{\mathbf{k}}\varepsilon(\mathbf{k})$ is the group velocity of the Bloch state with its energy dispersion $\varepsilon(\mathbf{k})$. The summation over the band index is omitted in Eq. (1) for simplicity. While the electron dynamics follow the semiclassical equation $\hbar\dot{\mathbf{k}} = -e(\mathbf{E} + \mathbf{v} \times \mathbf{B})$, the integral over time calculates the weighted average velocity over the past history of the electron orbit passing through \mathbf{k} ^{41,42}. The exponential weight guarantees the main contribution arising from the recent trajectory. Rolle's theorem allows us to approximate the time integral by the velocity at a particular past time $-\tau$ when the electron was located at $\mathbf{k}(-\tau)$ in the Brillouin zone. Thus, for every \mathbf{k} point, we are able to rewrite the time integral by keeping the leading term in the Taylor expansion as $\mathbf{v}[\mathbf{k}(-\tau)] = \mathbf{v}(\mathbf{k} - \dot{\mathbf{k}}\tau) \approx \mathbf{v}(\mathbf{k}) - \nabla_{\mathbf{k}}\mathbf{v}(\mathbf{k}) \cdot \left(-\frac{e\tau}{\hbar} \right) [\mathbf{E} + \mathbf{v}(\mathbf{k}) \times \mathbf{B}]$. Finally, we obtain the conductivity as

$$\sigma_{ij} = e^2 \tau \int \frac{d^3 k}{8\pi^3} v_i(\mathbf{k}) v_j(\mathbf{k}) \left(-\frac{\partial f}{\partial \varepsilon} \right)_{\varepsilon_F} + \frac{e^3 \tau^2}{\hbar} \int \frac{d^3 k}{8\pi^3} v_i(\mathbf{k}) [(\mathbf{v} \times \mathbf{B}) \cdot \nabla_{\mathbf{k}} v_j(\mathbf{k})] \left(-\frac{\partial f}{\partial \varepsilon} \right)_{\varepsilon_F}, \quad (2)$$

where the first term is the classic Drude conductivity independent of the magnetic field and the second term corresponds to the Hall effect due to the Lorentz force. Equation (2) is equivalent to the previous works derived from the Boltzmann transport equation^{37,43}.

With an in-plane magnetic field $\mathbf{B} = (B_x, B_y, 0)$, the Hall conductivity in Eq. (2) is explicitly simplified as

$$\sigma_{xy}^{\text{IPHE}} = \frac{e^3 \tau^2}{\hbar} \int \frac{d^3 k}{8\pi^3} v_x \left[\left(v_z \frac{\partial v_y}{\partial k_y} - v_y \frac{\partial v_y}{\partial k_z} \right) B_x + \left(v_x \frac{\partial v_y}{\partial k_z} - v_z \frac{\partial v_y}{\partial k_x} \right) B_y \right] \left(-\frac{\partial f}{\partial \varepsilon} \right)_{\varepsilon_F}. \quad (3)$$

Equation (3) provides a general but rigorous criterion to justify the presence of the IPHE. For the current in the (001) plane shown in Fig. 3h, the system has mirror symmetry about the z plane, as does the electronic velocity at the Fermi surface: $v_z(k_x, k_y, -k_z) = -v_z(k_x, k_y, k_z)$ and $v_{x,y}(k_x, k_y, -k_z) = v_{x,y}(k_x, k_y, k_z)$. Thus, every term in the integrand of Eq. (3) is an odd function of k_z , indicating that $\sigma_{xy}^{\text{IPHE}}$ always vanishes for an arbitrary in-plane field \mathbf{B} . By applying similar symmetry analysis, we can prove that the IPHE vanishes in the (100) and (110) planes of RuO₂.

For the RuO₂ (101) or IrO₂ (101) plane shown in Fig. 3k, the system has a glide mirror symmetry $\tilde{M}_y = \left\{ M_y \left| \frac{a}{2}, \frac{b}{2}, \frac{c}{2} \right. \right\}$, which imposes the following relationship of the Fermi velocity: $v_{x,z}(k_x, -k_y, k_z) = v_{x,z}(k_x, k_y, k_z)$ and $v_y(k_x, -k_y, k_z) = -v_y(k_x, k_y, k_z)$. Therefore, the integral of the second term is always zero, indicating that the B_y component does not contribute to the IPHE. In contrast, the B_x component induces a finite magnitude of $\sigma_{xy}^{\text{IPHE}}$, in agreement with the experimental observations in Fig. 1: the maximum Hall voltage at $\varphi = 0^\circ$ ($\mathbf{B} \parallel x$) and vanishing signal at $\varphi = 90^\circ$ ($\mathbf{B} \parallel y$). In addition, the in-plane Hall conductivity in Eq. (3) is linearly proportional to the applied magnetic field, and this proportionality perfectly agrees with the measured ρ_{xy} exhibiting a linear dependence on the magnetic field up to 8 Tesla (Fig. 2b). To confirm the symmetry analysis, we directly calculated the Hall conductivity using semiclassical electron dynamics, namely, Eq. (1), based upon the first-principles electronic structure^{41,42} (Fig. 4c and d). The calculated in-plane Hall conductivities for both RuO₂(101) and IrO₂(101) are both linearly proportional to the magnetic field (see the insets), and the calculated slope $K_{\text{ip}} = \rho_{xy}/B$ quantitatively reproduces the experimental values. The theoretical calculations again identify the Lorentz force as the dominant mechanism of the observed IPHE in the experiment.

Eq. (3) also indicates the symmetry requirements for a system to possess the IPHE: (1) The system does not have mirror symmetry M_z , twofold rotational symmetry C_{2z} , or their combination with time reversal, i.e., TM_z and TC_{2z} (for convenience, we use the notation S_z to represent an arbitrary symmetry in the set of $\{M_z, C_{2z}, TM_z, TC_{2z}\}$); (2) At least one of the S_x and S_y symmetries of the system is broken. For a material with S_x (S_y) broken, the in-plane Hall conductivity is proportional to B_x (B_y). If both S_x and S_y are broken, $\sigma_{xy}^{\text{IPHE}}$ becomes a combination of two terms, which are linear with B_x and B_y , respectively. The symmetry and the corresponding field dependence of the in-plane Hall conductivity are summarized in Fig. 4e. Note that even for highly symmetric systems, the derived constraints for the broken symmetry could be satisfied by certain film planes with large Miller indices. Thus, our analysis can significantly expand the material candidates with IPHE.

In addition to the Lorentz force, there is a possible contribution arising from the Berry curvature of the material resulting in $\rho_{xy}^{\text{IPHE}} \propto \tau^{-1}$ ³⁷. The slight decrease in ρ_{xy}^{IPHE} below 150 K may originate from the Berry curvature because of the relatively large relaxation time at low temperature. It is worth noting that the spatial symmetry requirements are the same for the in-plane Hall conductivity, regardless of whether the microscopic physical mechanisms are the Lorentz force or Berry curvature, but the contribution from Berry curvature needs to break the time reversal symmetry³⁷. All the materials with IPHE reported in the literature⁹⁻¹² satisfy the proposed symmetry constraint in Fig. 4e. The physical picture of the IPHE in altermagnetic RuO₂ and nonmagnetic IrO₂ can be readily generalized to the in-plane anomalous Hall effect in ferromagnetic materials with in-plane magnetization.

Conclusions

We have experimentally observed the IPHE in single-crystal rutile RuO₂(101) and IrO₂(101) films with the measured in-plane Hall resistivity nearly independent of temperature. The Hall resistivity is sensitively dependent on the direction of the applied in-plane magnetic field with respect to the crystal axes but is invariant to the current direction. These characteristics indicate that the Lorentz force provides the dominant mechanism to induce the IPHE, which is further quantitatively confirmed by first-principles calculations. The experimental observations are well captured by the microscopic description of the semiclassical electron dynamics, which allowed us to reveal the universal symmetry requirements for systems possessing the IPHE. Our results open an avenue to discover new material systems with the IPHE and expand the

understanding of the Hall effect.

References

- 1 Hall, E. H. On a New Action of the Magnet on Electric Currents. *Am. J. Math.* **2**, 287-292 (1879).
- 2 Zyuzin, V. A. In-plane Hall effect in two-dimensional helical electron systems. *Phys. Rev. B* **102**, 241105 (2020).
- 3 Wei, Y.-W., Feng, J. & Weng, H. Spatial symmetry modulation of planar Hall effect in Weyl semimetals. *Phys. Rev. B* **107**, 075131 (2023).
- 4 Wang, H. *et al.* Theory of Intrinsic In-Plane Hall Effect. arXiv:2211.05978 (2022).
- 5 Battilomo, R., Scopigno, N. & Ortix, C. Anomalous planar Hall effect in two-dimensional trigonal crystals. *Phys. Rev. Res.* **3**, L012006 (2021).
- 6 Tan, H., Liu, Y. & Yan, B. Unconventional anomalous Hall effect from magnetization parallel to the electric field. *Phys. Rev. B* **103**, 214438 (2021).
- 7 Cao, J. *et al.* In-Plane Anomalous Hall Effect in PT-Symmetric Antiferromagnetic Materials. *Phys. Rev. Lett.* **130**, 166702 (2023).
- 8 Cullen, J. H., Bhalla, P., Marcellina, E., Hamilton, A. R. & Culcer, D. Generating a Topological Anomalous Hall Effect in a Nonmagnetic Conductor: An In-Plane Magnetic Field as a Direct Probe of the Berry Curvature. *Phys. Rev. Lett.* **126**, 256601 (2021).
- 9 Li, P. *et al.* Anisotropic planar Hall effect in the type-II topological Weyl semimetal WTe₂. *Phys. Rev. B* **100**, 205128 (2019).
- 10 Liang, T. *et al.* Anomalous Hall effect in ZrTe5. *Nat. Phys.* **14**, 451-455 (2018).
- 11 Ge, J. *et al.* Unconventional Hall effect induced by Berry curvature. *Natl. Sci. Rev.* **7**, 1879-1885 (2020).
- 12 Zhou, J. *et al.* Heterodimensional superlattice with in-plane anomalous Hall effect. *Nature* **609**, 46-51 (2022).
- 13 Karplus, R. & Luttinger, J. M. Hall Effect in Ferromagnetics. *Phys. Rev.* **95**, 1154-1160 (1954).
- 14 Nagaosa, N., Sinova, J., Onoda, S., MacDonald, A. H. & Ong, N. P. Anomalous Hall effect. *Rev. Mod. Phys.* **82**, 1539-1592 (2010).
- 15 Jungwirth, T., Niu, Q. & MacDonald, A. H. Anomalous Hall Effect in Ferromagnetic Semiconductors. *Phys. Rev. Lett.* **88**, 207208 (2002).
- 16 Hoffmann, A. Spin Hall Effects in Metals. *IEEE Trans. Magn.* **49**, 5172-5193 (2013).
- 17 Sinova, J., Valenzuela, S. O., Wunderlich, J., Back, C. H. & Jungwirth, T. Spin Hall effects. *Rev. Mod. Phys.* **87**, 1213-1260 (2015).
- 18 Hirsch, J. E. Spin Hall Effect. *Phys. Rev. Lett.* **83**, 1834-1837 (1999).
- 19 Valenzuela, S. O. & Tinkham, M. Direct electronic measurement of the spin Hall effect. *Nature* **442**, 176-179 (2006).
- 20 Novoselov, K. S. *et al.* Room-Temperature Quantum Hall Effect in Graphene. *Science* **315**, 1379-1379 (2007).
- 21 Serlin, M. *et al.* Intrinsic quantized anomalous Hall effect in a moire heterostructure. *Science* **367**, 900-903 (2020).
- 22 Liu, C.-X., Zhang, S.-C. & Qi, X.-L. The Quantum Anomalous Hall Effect: Theory and Experiment. *Annu. Rev. Condens. Matter Phys.* **7**, 301-321 (2016).
- 23 Chang, C.-Z. *et al.* Experimental Observation of the Quantum Anomalous Hall Effect in a Magnetic Topological Insulator. *Science* **340**, 167-170 (2013).

24 Deng, Y. *et al.* Quantum anomalous Hall effect in intrinsic magnetic topological insulator MnBi₂Te₄. *Science* **367**, 895-900 (2020).

25 Wei, Y.-W., Li, C.-K., Qi, J. & Feng, J. Magnetoconductivity of type-II Weyl semimetals. *Phys. Rev. B* **97**, 205131 (2018).

26 Šmejkal, L., Sinova, J. & Jungwirth, T. Beyond Conventional Ferromagnetism and Antiferromagnetism: A Phase with Nonrelativistic Spin and Crystal Rotation Symmetry. *Phys. Rev. X* **12**, 031042 (2022).

27 Šmejkal, L., Sinova, J. & Jungwirth, T. Emerging Research Landscape of Altermagnetism. *Phys. Rev. X* **12**, 040501 (2022).

28 Šmejkal, L., González-Hernández, R., Jungwirth, T. & Sinova, J. Crystal time-reversal symmetry breaking and spontaneous Hall effect in collinear antiferromagnets. *Sci. Adv.* **6**, eaaz8809 (2020).

29 Feng, Z. *et al.* An anomalous Hall effect in altermagnetic ruthenium dioxide. *Nat. Electron.* **5**, 735-743 (2022).

30 González-Hernández, R. *et al.* Efficient Electrical Spin Splitter Based on Nonrelativistic Collinear Antiferromagnetism. *Phys. Rev. Lett.* **126**, 127701 (2021).

31 Bose, A. *et al.* Tilted spin current generated by the collinear antiferromagnet ruthenium dioxide. *Nat. Electron.* **5**, 267-274 (2022).

32 Bai, H. *et al.* Observation of Spin Splitting Torque in a Collinear Antiferromagnet RuO₂. *Phys. Rev. Lett.* **128**, 197202 (2022).

33 Karube, S. *et al.* Observation of Spin-Splitter Torque in Collinear Antiferromagnetic RuO₂. *Phys. Rev. Lett.* **129**, 137201 (2022).

34 Bai, H. *et al.* Efficient Spin-to-Charge Conversion via Altermagnetic Spin Splitting Effect in Antiferromagnet RuO₂. *Phys. Rev. Lett.* **130**, 216701 (2023).

35 Ky, V. D. Planar Hall Effect in Ferromagnetic Films. *Phys. Status Solidi B-Basic Res.* **26**, 565-569 (1968).

36 Seemann, K. M. *et al.* Origin of the Planar Hall Effect in Nanocrystalline Co₆₀Fe₂₀B₂₀. *Phys. Rev. Lett.* **107**, 086603 (2011).

37 Li, L., Cao, J., Cui, C., Yu, Z.-M. & Yao, Y. Planar Hall effect in topological Weyl and nodal line semimetals. arXiv:2304.09768 (2023).

38 Ping, Y., Galli, G. & Goddard, W. A., III. Electronic Structure of IrO₂: The Role of the Metal d Orbitals. *The Journal of Physical Chemistry C* **119**, 11570-11577 (2015).

39 Bose, A. *et al.* Effects of Anisotropic Strain on Spin-Orbit Torque Produced by the Dirac Nodal Line Semimetal IrO₂. *ACS Appl. Mater. Interfaces* **12**, 55411-55416 (2020).

40 Ashcroft, N. W. & Mermin, N. D. *Solid state physics*. Cengage Learning, (1976).

41 Liu, Y., Zhang, H.-J. & Yao, Y. Ab initio investigation of magnetic transport properties by Wannier interpolation. *Phys. Rev. B* **79**, 245123 (2009).

42 Yang, H. *et al.* Fully Band-Resolved Scattering Rate in MgB₂ Revealed by the Nonlinear Hall Effect and Magnetoresistance Measurements. *Phys. Rev. Lett.* **101**, 067001 (2008).

43 Ma, D., Jiang, H., Liu, H. & Xie, X. C. Planar Hall effect in tilted Weyl semimetals. *Phys. Rev. B* **99**, 115121 (2019).

Fig. 1

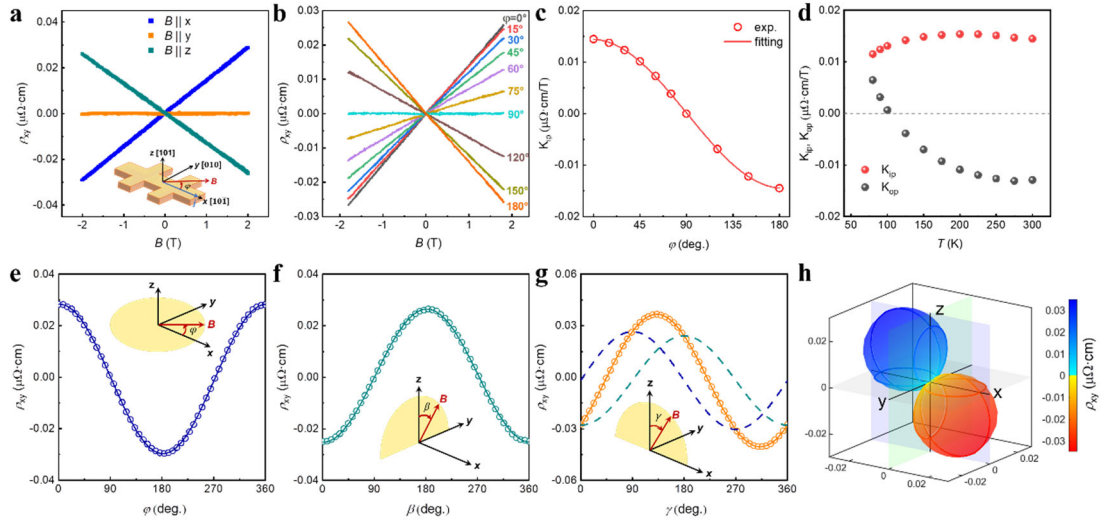


Fig. 1 | Transport measurements of the $\text{RuO}_2(101)$ thin film. **a**, Hall resistivity ρ_{xy} as a function of field along three orthogonal axes measured at 300 K. The current is along the $\text{RuO}_2[10\bar{1}]$ direction, and the film thickness is 10 nm. **b**, Field-dependent Hall resistivity with different in-plane field angles φ . **c**, φ -dependent slope of the Hall measurements in **b**. The data can be well fitted by the $\cos\varphi$ function. **d**, Temperature-dependent measurements of the IPHE and OHE. **e-g**, Field-angle dependence of Hall resistivity while rotating a field of 2 T in the x–y (**e**), y–z (**f**) and x–z (**g**) planes. Solid lines in **e** and **f** represent the fitting to a cosine function. The data in **g** can be decomposed as the superposition of an in-plane component (dashed blue line) and an out-of-plane component (dashed green line). **h**, The 3D polar plot of the angular dependence of the experimental Hall resistivity. Blue and red represent the positive and negative signs of the Hall resistivity, respectively.

Fig. 2

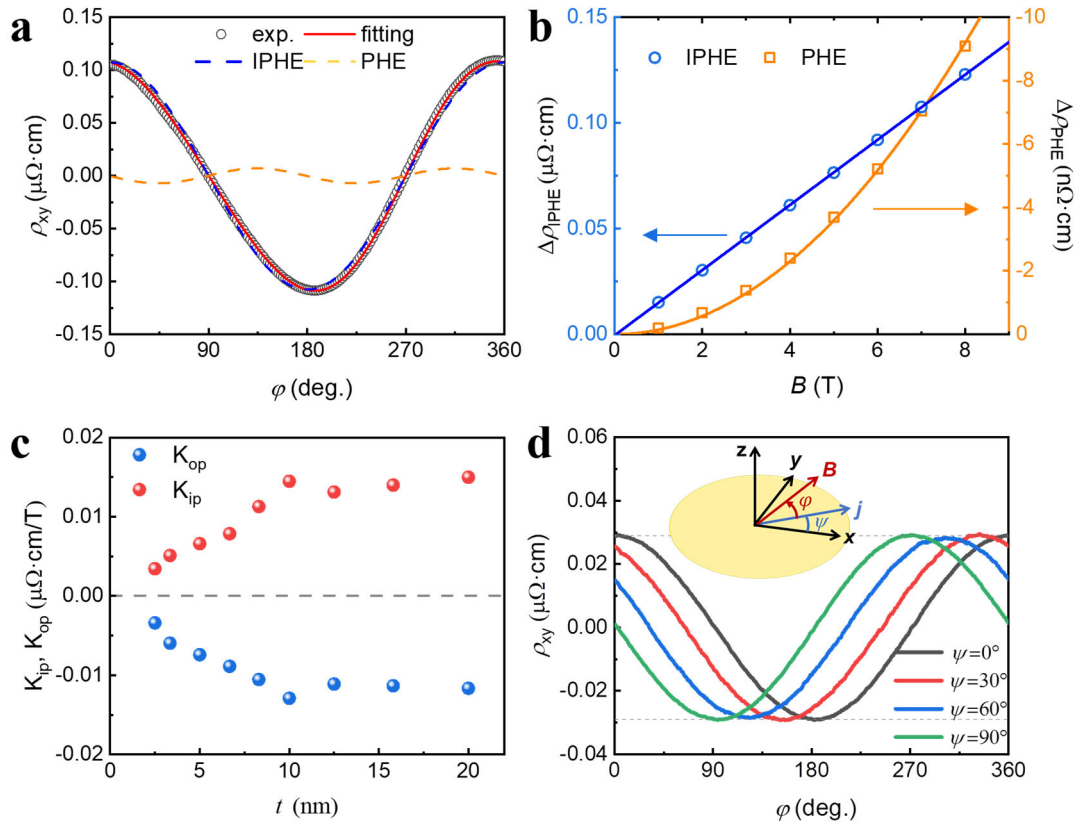


Fig. 2 | The angle- and thickness-dependent properties of the IPHE in RuO₂(101). **a**, A representative angle-dependent Hall resistivity measured under a magnetic field of 7 T rotating in the x-y plane. The blue and yellow dashed lines represent the fitting components of $\cos \varphi$ and $\sin 2\varphi$, respectively. **b**, The fitted magnitudes of IPHE and PHE as a function of magnetic field, which can be well fitted by the linear and quadratic functions, respectively. **c**, Thickness dependence of the slopes determined from the field-dependent IPHE and OHE measurements. **d**, IPHE measurements from devices with different current directions, where ψ refers to the angle of current j with respect to the RuO₂[101] axis.

Fig. 3

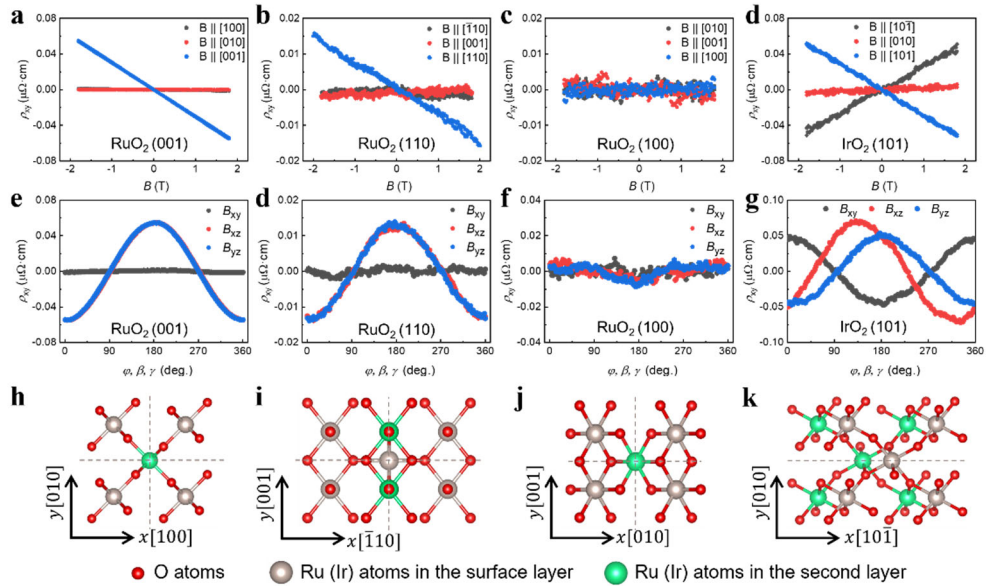


Fig. 3 | Hall measurements of rutile oxide films with different orientations. **a-d**, Field-dependent Hall resistivity with the field along three orthogonal directions for the samples RuO₂(001) (**a**), RuO₂(110) (**b**), RuO₂(100) (**c**) and IrO₂(101) (**d**). The thicknesses of all the films are 10 nm. The current in each experiment is along the x direction. **e-g**, Angular dependence of Hall resistivity with a rotating field of 1.8 T for the samples in **a-d**. **h-k**, Schematic diagrams of surface atomic structures for (001) (**h**), (110) (**i**), (100) (**j**) and (101) (**k**) rutile oxide films.

Fig. 4

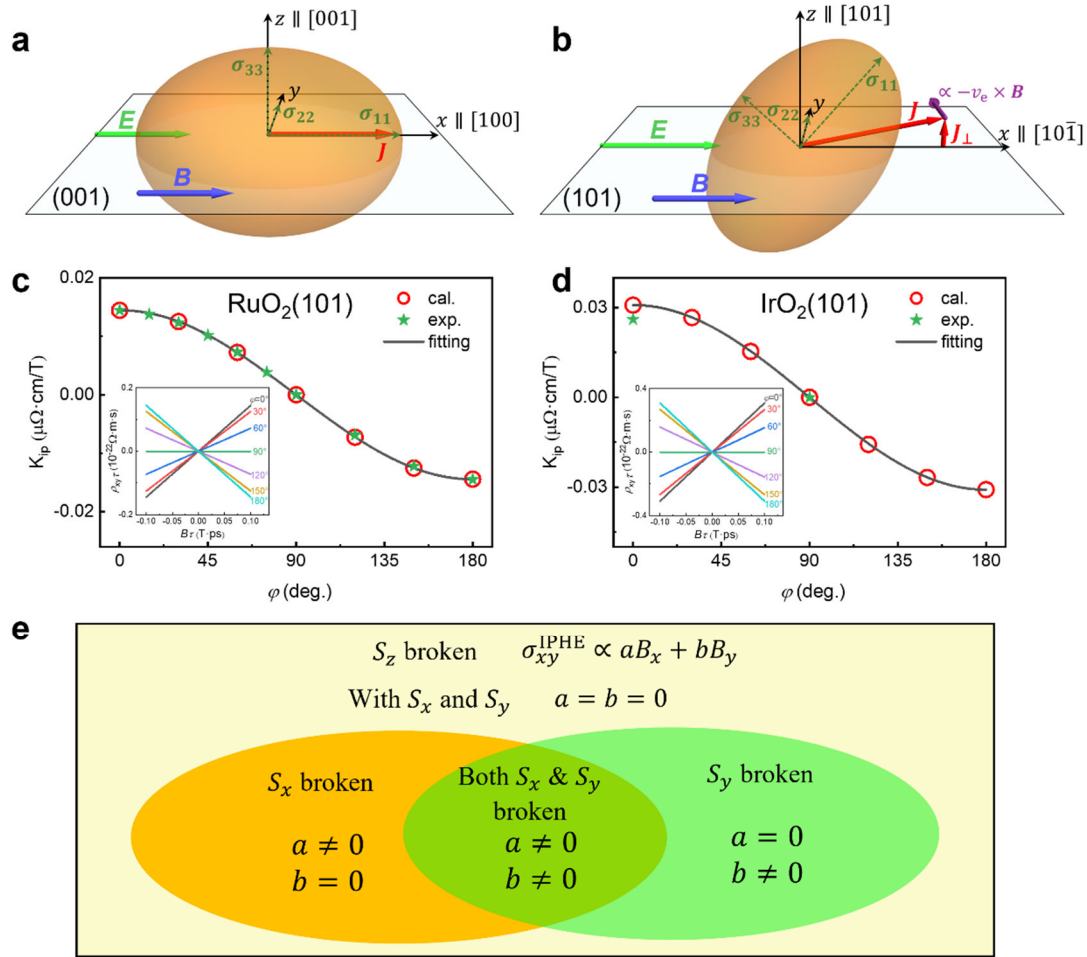


Fig. 4 | Physical picture of the IPHE in rutile oxide films and theoretical confirmation using first-principles calculations. **a**, Schematic illustration of the anisotropic conductivity in the $\text{RuO}_2(001)$ film. The current aligns with the electric field. **b**, Schematic illustration of the anisotropic conductivity in the $\text{RuO}_2(101)$ film. The current induced by the electric field along the $[10\bar{1}]$ axis contains a component perpendicular to the film. **c**, **d**, Calculated slope of the Hall resistivity to the in-plane magnetic field of RuO_2 and IrO_2 . The solid lines are the fitting to the angular dependence of $\cos \varphi$. The experimental values are plotted for comparison. Insets: Calculated $\rho_{xy}\tau$ as a function of $B\tau$ under the relaxation time approximation for different magnetic field directions. **e**, The symmetry constraint and the resulting field dependence of the IPHE.

1 **Methods**

2 **Sample preparation.**

3 Both RuO₂ (a=b=4.492 Å, c=3.106 Å) and IrO₂ (a=b=4.545 Å, c=3.19 Å) are
4 conductive rutile oxides, whose crystal structure is centrosymmetric with the space
5 group P4₂/mnm. Due to favourable lattice matching with TiO₂ (a=b=4.594 Å, c=2.969
6 Å), RuO₂ and IrO₂ films were epitaxially grown on single-crystal TiO₂ substrates by
7 DC magnetron sputtering at a substrate temperature of 500 °C in a high vacuum
8 chamber with a base pressure less than 2×10^{-8} Torr. Before deposition, the
9 substrates were pre-annealed at 500 °C for one hour in a vacuum chamber. During
10 deposition, the pressure in the chamber was maintained at 3 mTorr with a 4:1 ratio of
11 Ar and O₂. After RuO₂ or IrO₂ growth, the films were cooled to room temperature and
12 then capped with a 3 nm Al₂O₃ layer as a protection layer. The RuO₂(101) film can also
13 be epitaxially grown on an Al₂O₃ (1 $\bar{1}$ 02) substrate under the same growth conditions.
14 In addition, the growth of wedge-shaped samples was achieved by a motor that
15 controlled uniform movement of the front shutter, and the typical thickness slope was
16 ~3.3 nm/mm.

17
18 **Structural characterization.**

19 The film thickness and the microstructure were characterized at room temperature
20 by X-ray reflection (XRR) and X-ray diffraction (XRD) performed with an X-ray
21 diffractometer system using Cu K α radiation ($\lambda=1.5418$ Å). The deposition speed
22 specified by XRR is approximately 1.8 nm/min, and the roughness fitted by GENX
23 shown in the supplementary material is approximately 3.8 Å (Extended data Fig. 1a).
24 XRD patterns obtained from the θ -2 θ scan revealed that RuO₂ only has {101} peaks,
25 confirming that RuO₂ forms a rutile structure (Extended data Fig. 1b). The Φ -scan of
26 the {110} plane indicates a high crystallinity quality and the epitaxial relationship of
27 RuO₂(101) [010]/TiO₂ (101) [010]. Here, Φ is the azimuthal rotation angle (Extended
28 data Fig. 1c). In addition, XRD measurements were also performed on RuO₂(001),
29 (110), (100) and IrO₂ (101) samples (Extended data Fig. 3). The high-quality growth of
30 the RuO₂(101) film was also confirmed by reflection high-energy electron diffraction
31 (RHEED) measurements, which were performed in a UHV system with the electron
32 beam directed along the [010] direction. The clear elongated spots in the RHEED
33 pattern also demonstrate the epitaxial growth of the RuO₂ films (Extended data Fig. 1d).

34 The crystalline response of the RuO₂ film along the [10 $\bar{1}$] and [010] was also
35 examined by cross-sectional scanning transmission electron microscopy (STEM). From
36 the high-resolution high-angle annular dark field (HAADF) STEM images, the
37 morphology of the RuO₂ film is continuous and epitaxial to the TiO₂ substrate
38 (Extended data Fig. 1e and f). The cross-section TEM samples were prepared by a dual-

39 beam scanning electron microscope (ThermoFisher Scientific, Helios G4 CX). The
40 final milling step of the fabrication was performed under a 5 kV ion beam voltage to
41 reduce surface damage. The aberration-corrected TEM (ThermoFisher Scientific, Titan)
42 with a 300 kV accelerating voltage was used to reveal the crystal structure of the
43 samples.

44

45 **Transport measurements.**

46 For the electrical measurements, films were patterned into Hall–bar devices with
47 a length of 600 μm and a width of 150 μm through standard photolithography and Ar-
48 ion etching. Electric contacts are made of a 10-nm-thick Cr layer covered by a 100-nm-
49 thick Au layer. The Hall resistance measurements were carried out by a standard four-
50 probe method. In the transport measurements, the amplitude of the applied AC current
51 was fixed at 2 mA with an oscillating frequency of 17.3 Hz, and the voltage signals
52 were detected by a lock-in amplifier. The measured Hall resistivity is independent of
53 the current density (Extended data Fig. 7). Most of the Hall measurements shown in
54 this study were performed in a three-dimensional vector superconducting magnet
55 system (Cryogenics), where a magnetic field up to 2 Tesla can be aligned in an arbitrary
56 direction. The Hall resistivity under a field larger than 2 Tesla was obtained in a
57 commercial physical property measurement system (PPMS, Quantum Design).

58 The transport measurements were performed on a 10 nm RuO₂(101) film grown
59 on an Al₂O₃(1 $\bar{1}$ 02) substrate, which gives the same results as those on the RuO₂(101)
60 films grown on a TiO₂(101) substrate (Extended data Fig. 8).

61

62 **First-principles calculations.**

63 The electronic structures of RuO₂ and IrO₂ are calculated self-consistently based
64 upon density functional theory implemented in the Vienna Ab initio Simulation Package
65 (VASP)^{1,2}. The electron–ion interactions were described by the projector augmented
66 wave (PAW) method^{3,4}, and the exchange–correlation functional was modelled by the
67 generalized gradient approximation within the framework of Perdew–Burke–Ernzerhof
68 (PBE)⁵. The valence electron configurations for Ru, Ir and O atoms were chosen as
69 4p⁶4d⁷5s¹, 5d⁸6s¹, and 2s²2p⁴, respectively. The correlation effects of the 4d orbitals of
70 Ru and the 5d orbitals of Ir were taken into account by including the effective on-site
71 Hubbard U of 1.2 eV and 1.6 eV, respectively⁶. The calculated wave functions were
72 expanded in plane-wave basis with an energy cut-off of 600 eV, and a 16 \times 16 \times 24 k -
73 mesh was employed to sample the Brillouin zone. The maximally localized Wannier
74 functions (MLWFs) were constructed using the WANNIER90 code^{7,8}, and the in-plane
75 Hall effect (IPHE) calculations of RuO₂ and IrO₂ were performed by solving the
76 equation for the semiclassical electronic dynamics at the Fermi surface^{9,10} with a fine

77 mesh of 90×90×90 points to sample the Brillouin zone.

78

79 **References:**

80 1 Kresse, G. & Furthmüller, J. Efficient iterative schemes for ab initio total-energy
81 calculations using a plane-wave basis set. *Phys. Rev. B* **54**, 11169-11186 (1996).

82 2 Kresse, G. & Furthmüller, J. Efficiency of ab-initio total energy calculations for metals and
83 semiconductors using a plane-wave basis set. *Computational Materials Science* **6**, 15-50
84 (1996).

85 3 Kresse, G. & Joubert, D. From ultrasoft pseudopotentials to the projector augmented-
86 wave method. *Phys. Rev. B* **59**, 1758-1775 (1999).

87 4 Blöchl, P. E. Projector augmented-wave method. *Phys. Rev. B* **50**, 17953-17979 (1994).

88 5 Perdew, J. P., Burke, K. & Ernzerhof, M. Generalized Gradient Approximation Made Simple.
89 *Phys. Rev. Lett.* **77**, 3865-3868 (1996).

90 6 Dudarev, S. L., Botton, G. A., Savrasov, S. Y., Humphreys, C. J. & Sutton, A. P. Electron-
91 energy-loss spectra and the structural stability of nickel oxide: An LSDA+U study. *Phys.*
92 *Rev. B* **57**, 1505-1509 (1998).

93 7 Mostofi, A. A. *et al*. wannier90: A tool for obtaining maximally-localised Wannier functions.
94 *Computer Physics Communications* **178**, 685-699 (2008).

95 8 Mostofi, A. A. *et al*. An updated version of wannier90: A tool for obtaining maximally-
96 localised Wannier functions. *Computer Physics Communications* **185**, 2309-2310 (2014).

97 9 Liu, Y., Zhang, H.-J. & Yao, Y. Ab initio investigation of magnetic transport properties by
98 Wannier interpolation. *Phys. Rev. B* **79**, 245123 (2009).

99 10 Yang, H. *et al*. Fully Band-Resolved Scattering Rate in MgB₂ Revealed by the Nonlinear
100 Hall Effect and Magnetoresistance Measurements. *Phys. Rev. Lett.* **101**, 067001 (2008).

101

102

103 **Acknowledgements**

104 The work was supported by the National Key Research and Development Program of
105 China (2022YFA1403300), the National Natural Science Foundation of China (Grant
106 No. 11974079, No. 12274083, No. 12221004, No. 12174028, No. 52231007, No.
107 51725101, and No. 11727807), the Shanghai Municipal Science and Technology Major
108 Project (Grant No. 2019SHZDZX01), the Shanghai Municipal Science and Technology
109 Basic Research Project (No. 22JC1400200), and the Ministry of Science and
110 Technology of China (2021YFA1200600 and 2018YFA0209100).

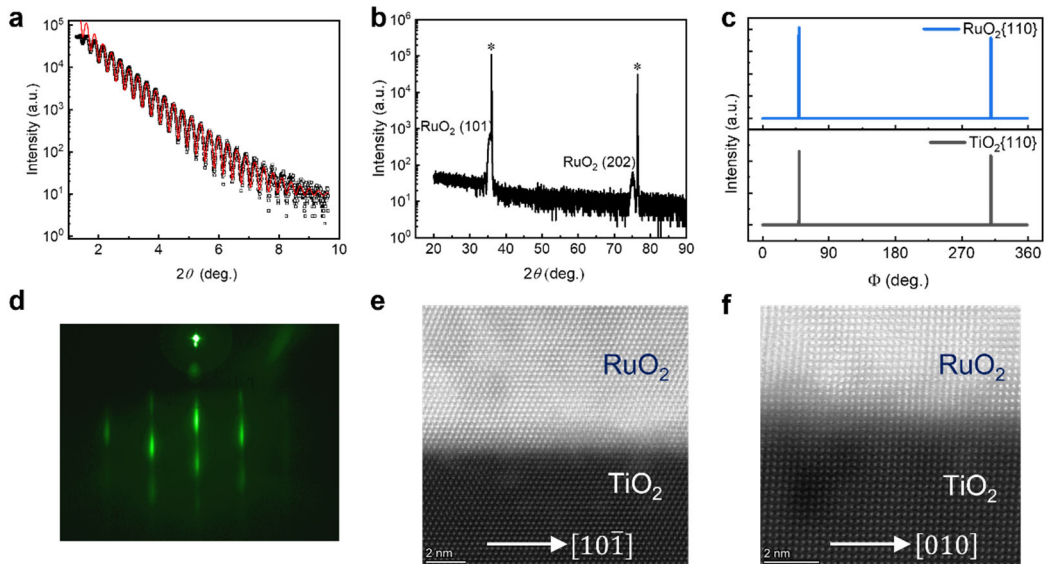
111

112 **Author contributions**

113 Y. Cui, Yiz. W., and Z. Y. conceived the ideas and supervised the project. Y. Cui grew
114 the samples and fabricated the devices. Y. Cui, Yunz. W., and H. C. performed the
115 transport measurements. Y. Cui, Yunz. W., H. C., N. X. and X. Q. performed the XRD
116 experiments. K. P. and R. C. performed the TEM measurements. Y. L. developed the
117 computational program to calculate the electrical conductivity. Z. L., Y. Chen, and Z.
118 Y. conducted the first-principles calculations and performed the symmetry analysis. Y.
119 Cui, Yiz. W. and Z. Y. wrote the manuscript. All the authors participated in the
120 discussions.

121

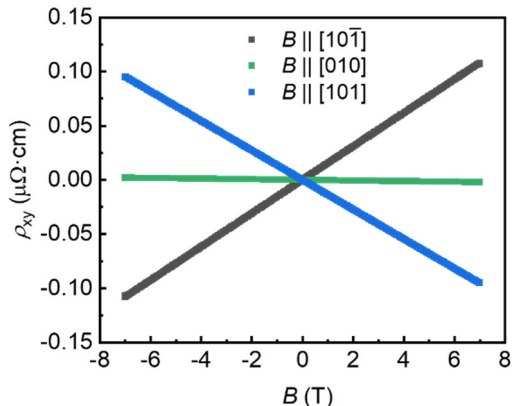
122



123

124

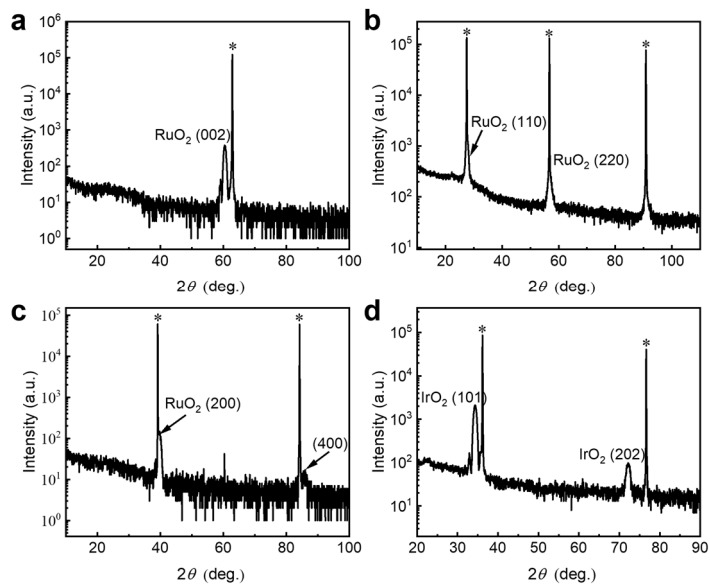
125 **Extended Data Fig. 1 | Structural characterization of RuO₂(101) films grown on a**
 126 **TiO₂ (101) substrate.** **a-b,** XRR spectra and θ - 2θ scan spectra of the RuO₂ film. The
 127 symbol * marks the peaks from the TiO₂ (101) substrate. **c,** Φ -scan spectra of the
 128 noncleavage plane of RuO₂ and the TiO₂ substrate. **d,** RHEED pattern from a 10 nm-
 129 thick RuO₂ (101) film grown on a TiO₂ (101) substrate. The electrons are incident along
 130 the RuO₂ [010] direction. **e-f,** High-resolution annular dark-field scanning transmission
 131 electron microscopy images of the (101) plane.
 132



133

134

135 **Extended Data Fig. 2** | The field-dependent Hall resistivity of a 10 nm-thick RuO₂(101)
 136 sample under a magnetic field up to 7 T along the [10̄1], [010], and [101] directions.
 137

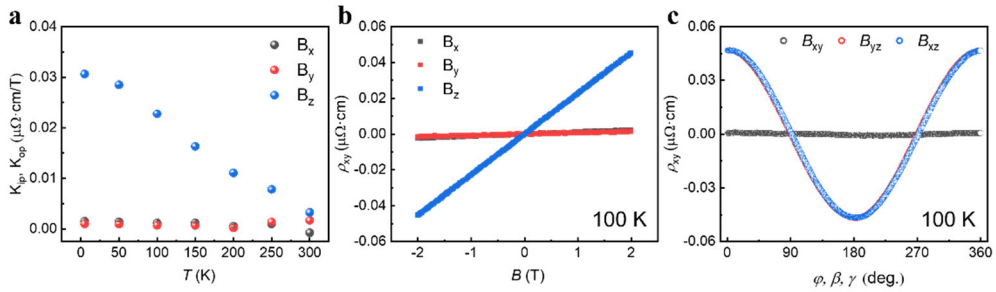


138

139

140 **Extended Data Fig. 3 | Structural characterization of RuO_2 and IrO_2 films with**
 141 **different crystal orientations.** a-d, θ - 2θ scan spectra of RuO_2 films with (100) (a),
 142 (110) (b), and (001) (c) orientations grown on the corresponding TiO_2 substrates, as
 143 well as IrO_2 (101) films grown on TiO_2 (101) (d). The symbol * marks the peaks from
 144 the substrates.

145

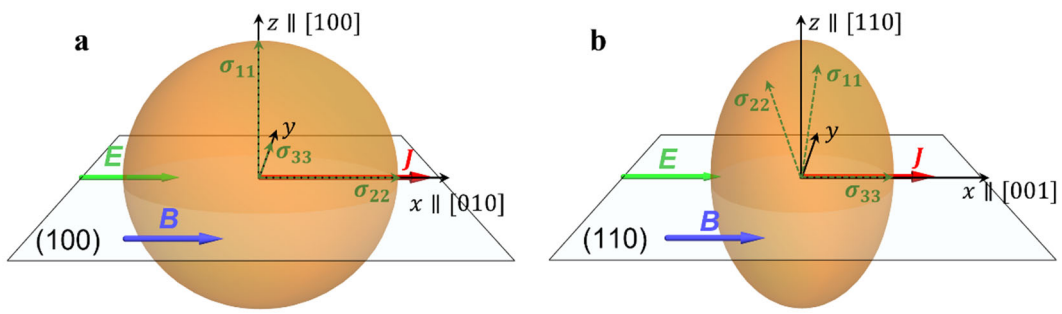


146

147

148 **Extended Data Fig. 4 | Temperature dependence in RuO₂ (100).** **a**, the measured
 149 Hall coefficients as a function of temperature when the magnetic field is applied to x, y
 150 and z, respectively. The definition is shown in Fig. 3. **b**, Magnetic field-dependent
 151 resistivity in the three typical directions at 100 K. **c**, Angular dependence of the Hall
 152 resistivity in three field-rotating planes at 100 K.

153

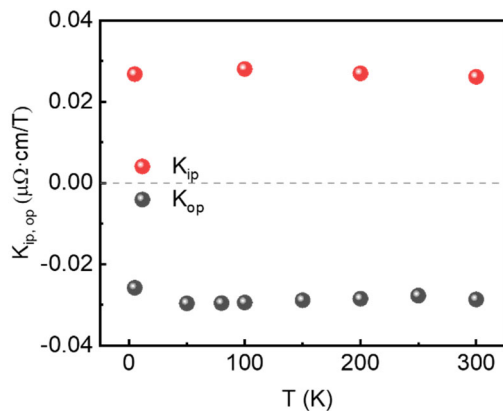


154

155

156 **Extended Data Fig. 5** | Schematic diagram of the Hall effect in RuO₂ (100) (a) and
 157 RuO₂ (110) (b). No in-plane Hall effect was observed in these two crystal planes due
 158 to the cancellation of the Lorentz force.

159



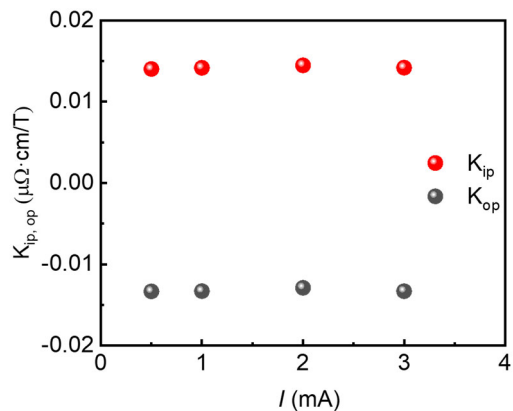
160

161

162 **Extended Data Fig. 6** | Temperature dependence of K_{ip} and K_{op} measured for a 10 nm-thick $\text{IrO}_2(101)$ film grown on a $\text{TiO}_2(101)$ substrate.

163

164

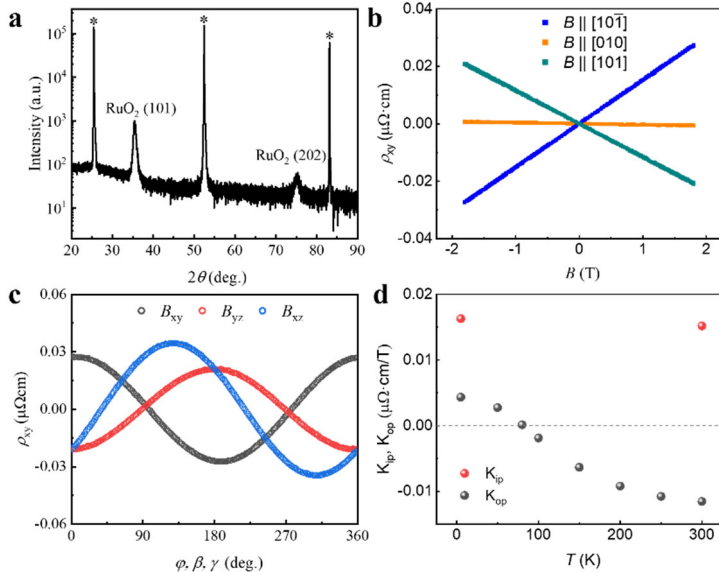


165

166

167 **Extended Data Fig. 7** | The relationship of the IPHE and OHE on the current magnitude
168 in a 10 nm RuO₂ (101) sample.

169



170

171

172 **Extended Data Fig. 8 | The IPHE and OHE in a 10 nm-thick RuO₂(101) film grown**
 173 **on an Al₂O₃(1102) substrate.** **a**, θ -2 θ scan spectra of the RuO₂ film. The symbol *
 174 marks the peaks from the substrates. **b**, Magnetic field-dependent Hall resistivity with
 175 the field along the three typical directions at 300 K. **c**, Angular dependence of the Hall
 176 resistivity under the magnetic field rotated in three planes at 300 K. **d**, The temperature
 177 dependence of the coefficients K_{ip} and K_{op}.

178